CHAPTER 5

The sea ice–ocean boundary layer

Miles G. McPhee

McPhee Research Company, Naches, WA, USA

5.1 Introduction

Sea ice exerts profound influence on air–sea interaction by effectively insulating the upper ocean from the cold polar atmosphere, thus reducing both outgoing long-wave radiation and sensible heat exchange, and by drastically changing the surface albedo, inhibiting the oceanic absorption of shortwave radiation. There is often shear (relative motion) between the ice and underlying ocean, either in response to wind forcing in the extensive ice packs of polar oceans, or from tidally induced currents or other circulation under shorefast ice. The shear induces a boundary layer beneath the ice in which transfers of momentum, heat and salt are controlled by turbulent exchange processes. This ice–ocean boundary layer (IOBL) shares many characteristics with open ocean boundary layers, except that the upper boundary conditions are imposed by a solid–liquid interface instead of a gas–liquid interface, and as a consequence surface gravity waves play a minor role in IOBL dynamics, except in marginal ice zones or with low ice concentrations.

In the open ocean, vertical displacements and orbital velocities from surface waves present a formidable obstacle to direct measurement of turbulent fluxes. In contrast, drifting pack ice presents a stable measurement platform, often moving with the maximum velocity in the water column, from which it is relatively easy to deploy clusters of instruments through the entire extent of a rotating planetary boundary layer. Since the 1970s, the 'laboratory' aspects of drifting sea ice have been exploited to measure the small deviatory changes in velocity and scalar properties necessary for covariance estimates of turbulent (Reynolds) fluxes. Coupled with

modern techniques for measuring profiles of temperature, salinity and velocity (by acoustic profiler) on a more or less continuous basis for weeks or months at a time, this has provided us an unprecedented view of how the IOBL works, and much insight into planetary boundary layers in general.

Ice-covered polar oceans are cold, often quite near their salinity-determined freezing temperatures, with small temperature contrast between the upper ocean and the base of the ice cover. Compared with instantaneous radiative and even turbulent convective exchanges at the upper surface of the ice, instantaneous ocean (basal) heat flux magnitudes are generally modest, yet Maykut and Untersteiner (1971) found in their thermodynamic sea ice model that about 2 W m^{-2} heat flux from the ocean was required to maintain a steady-state ice thickness. Nevertheless, during the initial planning stages for the year-long Surface Heat Budget of the Arctic (SHEBA) project, some participants questioned the necessity of measuring ice–ocean exchanges at all. As it turned out, our measurements over the SHEBA year demonstrated much variability in basal heat flux, with the annual average of about 7.2 W m^{-2} (McPhee, 2008b; Shaw et al., 2009), coinciding closely with the heat absorbed by a net ice loss of about 75 cm at the SHEBA station reported by Perovich et al. (2003). Clearly, it is important to understand exchanges between the ice and ocean, particularly in a time when the state of the ice pack appears to be rapidly changing.

There are two main themes in this chapter. Section 5.2 investigates the structure of the IOBL, mainly from the standpoint of scales that govern turbulent transfer with emphasis on the drag relationship required for estimating interface transfers of heat and salt as well

as momentum. Section 5.3 deals with the immediate ice–ocean interface from the perspective of the ocean. It emphasizes the role played by salt in controlling transfer rates through an infinitesimal control volume following the interface, and formulates boundary conditions for underlying turbulent boundary layer.

5.2   Turbulent exchange in the IOBL

Sea ice (as well as floating glacial ice) interacts with the ocean through a turbulent boundary layer influenced directly by rotation. During the 1893–1896 *Fram* expedition, F. Nansen noted that the vessel consistently drifted in a direction 20–40° clockwise from the surface wind, which he surmised was an obvious manifestation of the Earth's rotation. A young Swedish researcher, V.W. Ekman (1905), working with Nansen and V. Bjerkness, solved the fluid equations with friction in a rotating reference frame, in the process discovering an elegantly simple spiral structure for velocity in the upper ocean forced by stress at the surface. In his truly remarkable paper, Ekman not only deduced the velocity spiral that now bears his name, but also foretold the presence of inertial oscillations, and laid the foundation for understanding coastal upwelling and storm surges.

Despite ample indirect evidence for Coriolis deflection of winds in the atmospheric boundary layer gathered during the first half of the 20th century, the first unequivocal example of an Ekman spiral in nature was published by Hunkins (1966) from a composite of current profiles measured under pack ice over a 2-month period at Arctic Drift Station Alpha during the International Geophysical Year in 1958. Subsequently, numerous measurements made from drifting sea ice have demonstrated spiral-like IOBL structures, in both velocity (e.g. McPhee & Smith, 1976) and turbulent Reynolds stress (McPhee & Martinson, 1994). In spite of the significant logistical barriers to operating in polar oceans, the unique capability for measuring from a stable platform at the surface, without the complicating impact of surface gravity waves (with significant orbital velocities and platform motion), has provided much insight into how turbulent exchange in rotating boundary layers occurs. In this respect, the IOBL studies carry on a tradition founded by Nansen and Ekman.

5.2.1   Basic equations

Equations most pertinent to ice–ocean interaction are derived from basic conservation equations for momentum, heat and salt, and are well presented in standard oceanographic texts (Gill, 1982; Pedlosky, 1987). Derivations specifically for the IOBL are found in McPhee (2008b; Chapter 2). For fully developed turbulence in natural planetary boundary layers (i.e. in a rotating reference frame attached to Earth), the Bousinesq form of the momentum equation (ignoring molecular diffusion but not friction) may be written

$$\frac{\partial \boldsymbol{u}}{\partial t} + \boldsymbol{u} \cdot \nabla \boldsymbol{u} + f \boldsymbol{k} \times \boldsymbol{u} = -\nabla p/\rho - g\frac{\rho'}{\rho}\boldsymbol{k} + \nabla \cdot \underset{\sim}{\tau} \quad (5.1)$$

where $\boldsymbol{u}$ is vector velocity of the *mean* flow (i.e. slowly varying in comparison with turbulent fluctuations); $f = 2\omega \sin \phi$ is the Coriolis parameter (ϕ is latitude, $\omega = 7.292 \times 10^{-5}$ s^{-1} is Earth's angular rotation speed); ∇p is the large-scale pressure gradient; ρ' is a small density perturbation from the background density; and g is the acceleration due to gravity. The last term in equation (5.1) is not viscous stress divergence (which would normally be expressed as $\nu\nabla^2\boldsymbol{u}$), but rather the divergence of the Reynolds stress tensor, which follows from applying the Reynolds decomposition ($\boldsymbol{U} = \boldsymbol{u} + \boldsymbol{u}'$ where $\boldsymbol{U}$ is total velocity) to the advective term $\boldsymbol{U} \cdot \nabla \boldsymbol{U}$. The components of Reynolds stress tensor are:

$$\tau_{ij} = -\langle u_i' u_j' \rangle$$

Summing the trace of $\underset{\sim}{\tau}$, ($\langle u_i' u_i' \rangle$ repeated indices imply summation) yields twice the turbulent kinetic energy per unit mass. Usually, the main interest for turbulent exchange is the vertical derivative of a horizontal traction vector:

$$\begin{aligned}\boldsymbol{\tau} &= -\langle u'w' \rangle \boldsymbol{e}_x - \langle v'w' \rangle \boldsymbol{e}_y \\ &= -\langle u'w' \rangle - i\langle v'w' \rangle\end{aligned} \quad (5.2)$$

where the second representation expresses the two-dimensional vector as a complex number with the x-component along the real axis and the y-component along the imaginary axis.

The pressure gradient term in equation (5.1) provides a definition of geostrophic current

$$f\mathbf{k} \times \mathbf{v}_g = -g\nabla\eta \quad (5.3)$$

where η is sea-surface elevation. The same pressure gradient term acts on drifting sea ice, so in a state with no

other forcing (e.g. no wind stress or ice stress gradient), the upper ocean and ice will drift with u_g, and there will be no shear to generate turbulence. It is thus often convenient to express the boundary layer equations in terms of horizontal velocity relative to geostrophic flow, eliminating the large-scale pressure gradient term:

$$\frac{\partial u}{\partial t} + u \cdot \nabla u + f k \times u = \nabla \cdot \underset{\sim}{\tau} \qquad (5.4)$$

Similar conservation equations may be derived for scalar IOBL properties. For heat (temperature):

$$\frac{\partial T}{\partial t} + u \cdot \nabla T = Q^H/(\rho c_p) \qquad (5.5)$$

where Q^H is a heat source within the IOBL (e.g. solar heating), and c_p is the specific heat of seawater. For temperatures near freezing, c_p is close to $4\,kJ\,kg^{-1}\,K^{-1}$ (see Gill, 1982, table A3.1). A similar conservation equation for salinity is:

$$\frac{\partial S}{\partial t} + u \cdot \nabla S = Q^S/\rho \qquad (5.6)$$

where for generality a source term for salinity is included (a possible source might be from nucleation of frazil crystals).

5.2.2 Impacts of rotation

If IOBL flow is steady and horizontally homogeneous, equation (5.4) is simply:

$$if u = \frac{\partial \tau}{\partial z} \qquad (5.7)$$

where $u = u + iv$ in complex notation. At some level near the far extent of the boundary layer, turbulent stress approaches zero, so integrating equation (5.7) from that level to the surface:

$$if \int_{Z_{bl}}^{0} u\,dz = if M = \tau_0 \qquad (5.8)$$

where M is the vector volume transport in the IOBL and τ_0 is kinematic stress at the boundary. Thus in a steady state, average transport is at right angles to the stress (clockwise in the northern hemisphere), regardless of the details of turbulence in the IOBL. A shallow layer requires higher mean velocity than a deep layer to effect the same transport, which places an important constraint on IOBL scales.

By vector manipulation of equation (5.8) with the addition of the continuity equation, it follows that:

$$\nabla \cdot M = w_{EP} \approx \frac{1}{f} \nabla \times \tau_0 \qquad (5.9)$$

where w_{EP} is vertical (Ekman pumping) velocity at the base of the mixed layer relative to the surface. Over the past few decades, late summer (August–October) wind stress curl over the Canada Basin (western Arctic) has become increasingly negative, resulting in convergence of near surface water (McPhee, 2013). Freshwater from more intense ice melt and continental run-off is herded by the stress curl mechanism toward the center of the Beaufort Gyre, resulting in stronger stratification (shallower mixed layers) and increased sea-surface elevation gradients. Disappearance of perennial pack ice in the Canada Basin (Maslanik et al., 2011; Nghiem et al., 2007) appears to have been strongly influenced by more intense currents in the Beaufort Gyre, which in turn are linked directly to the stress curl via equation (5.9) (McPhee, 2013).

Besides relating stress and volume transport, equation (5.8) reveals little about the structure of currents and momentum flux in the IOBL. Ekman (1905) addressed equation (5.7) by positing that stress and velocity were related by an 'eddy viscosity' that behaved like kinematic viscosity (which depends on the molecular velocity times mean free path) except at much larger scales. His elegant solution revealed a spiral in current structure, in which surface velocity veered 45° to the right of surface stress, seemingly explaining Nansen's drift observations. It is sometimes overlooked that Ekman considered eddy viscosity to be constant only with respect to the vertical dimension. Based partly on the setup of coastal currents during storms, he postulated that it should vary as the square of wind speed (i.e. the surface stress) and suggested quantitative values not far different from what we have subsequently measured with modern instrumentation.

Boundary layer currents measured under drifting pack ice often exhibit what may be interpreted as Ekman spirals. An example from a storm during the Arctic Ice Dynamics Joint Experiment (AIDJEX) Pilot Study in 1972 (Figure 5.1a) shows current vectors at several levels drawn with respect to the current measured at 32 m, where the absolute current was small (McPhee & Smith, 1976). The reference frame was chosen so that the stress acting on the IOBL was in the negative x direction. Profiles in Figure 5.1(b) show that although the surface velocity was largely dominated by the shear between the interface and 2 m level, the integrated transport in the direction of
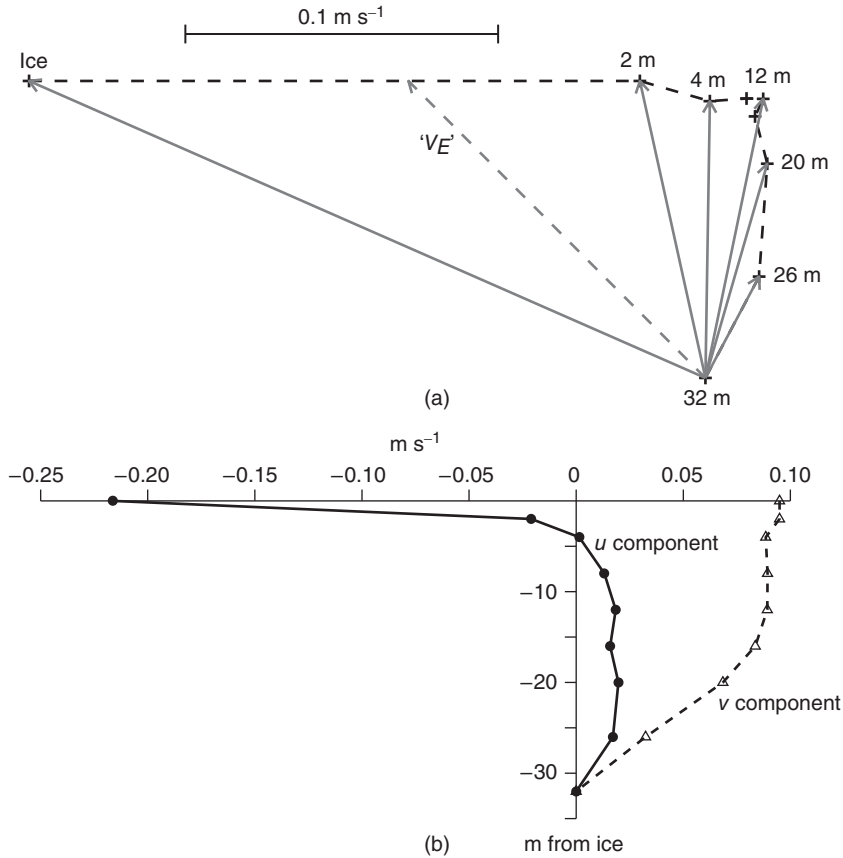
0.1 m s^{-1}

Ice

2 m 4 m 12 m

'V$_E$'

20 m

26 m

(a)   32 m

m s^{-1}

−0.25   −0.20   −0.15   −0.10   −0.05   0   0.05   0.10

u component

−10

−20

v component

−30

(b)   m from ice

Figure 5.1 (a) Plan view of currents measured for 5 hours during a storm at the 1972 Arctic Ice Dynamics Joint Experiment (AIDJEX) Pilot Study site. All currents are shown relative to the current measured at 32 m. The dashed vector is drawn where the velocity is 45° clockwise from the surface stress. (b) Current profiles with the x-axis aligned antiparallel to the surface stress.

stress was near zero. The dashed vector labelled 'V_E' lies 45° clockwise from surface stress and falls within the upper 2 m. Turbulent stress at that level is nearly the same as at the interface, so this can be taken as the upper limit of the Ekman spiral. Basic aspects of Ekman turning are nearly always present to some degree in our measurements from drifting ice. A further example, this one from the southern hemisphere (Figure 5.2), was constructed from hundreds of hours of acoustic Doppler current profiler current data obtained during the Ice Station Polarstern (ISPOL) project in the western Weddell Sea (McPhee, 2008a). The vectors shown were formed by non-dimensionalizing (by complex division) 3 hour samples of currents at 2 m intervals from 10 to 28 m by the current measured at 30 m, then averaging all of the non-dimensional profiles.
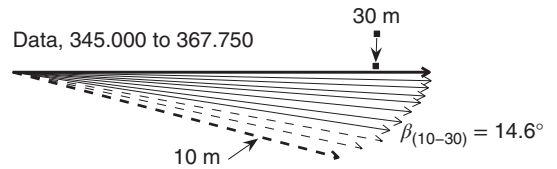

Data, 345.000 to 367.750

30 m

$\beta_{(10–30)} = 14.6°$

10 m

Figure 5.2 Average non-dimensional current hodograph (plan view) of complex currents measured relative to drifting ice, sampled every 2 m from 10 to 28 m, after dividing by the current at 30 m. Source: Adapted from McPhee, 2008a. Reproduced with permission of Elsevier.

5.2.3 Inertial oscillation

Ekman (1905, with credit to Fredholm) also presented a solution to the time-dependent problem, showing circular currents oscillating with a period of a 'half-pendulum day' ($2\pi/f$) about the mean currents of the steady solution. A much simplified illustration of

these circular currents follows from the time-dependent version of the horizontally homogeneous volume transport equation:

$$\frac{\partial M}{\partial t} + ifM = \tau_0 \qquad (5.10)$$

If the upper ocean initially at rest is subjected to an impulsive stress in the imaginary (y) direction, $i\tau_0$, at time $t = 0$, the complex solution to equation (5.10) is:

$$M = \frac{\tau_0}{f}(1 - e^{-ift})$$

tracing a circle in the complex plane in one inertial period (half-pendulum day) about the steady-state balance $M_{ss} = \tau_0/f$. Because there is no friction in the system, it continues to oscillate about M_{ss}, but never reaches the steady-state value. While this might seem patently unrealistic, it is useful to consider some numbers. Kinematic surface stress from a fast-moving atmospheric system near the North Pole might have a magnitude $\tau_0 = 2 \times 10^{-4} \text{m}^2\text{s}^{-2}$ with maximum volume transport (at $t = 6, 18, 30\,\text{h}$, etc.) of about $2.75\,\text{m}^2$ s^{-1}. If the summer mixed layer was $25\,\text{m}$ thick, the depth-averaged velocity would be around $11\,\text{cm s}^{-1}$.

Satellite tracking of ice motion often shows 'scallops' in drift trajectories, indicating cycloidal motion, particularly in summer when mixed layers tend to be shallow and internal ice forces small. An example from an unmanned buoy, initially deployed near the North Pole (Figure 5.3), shows that for about four inertial periods beginning at time 270.0 (year day 2002), the buoy trajectory can be reasonably reproduced by integrating the simple expression for velocity, comprising a mean drift plus an inertial oscillation as listed in the figure. The mean ice velocity is dominated by shear between the ice cover and upper mixed layer in the direction of surface stress, so the actual velocity in the mixed layer was probably not much different from the highly idealized example above.

Given a time series of drift positions, complex demodulation provides a useful means of separating inertial (or tidal) components of ice drift from the underlying mean motion. The technique, described in detail by McPhee (1988, 2008b), involves fitting the observed positions to basis functions comprising preferred inertial and/or tidal frequencies, for example:

$$X(t) = X_0 + V_0 t + (i/f)\,[S_{cw}(e^{-ift} - 1) + S_{ccw}(1 - e^{ift})] + \dots$$

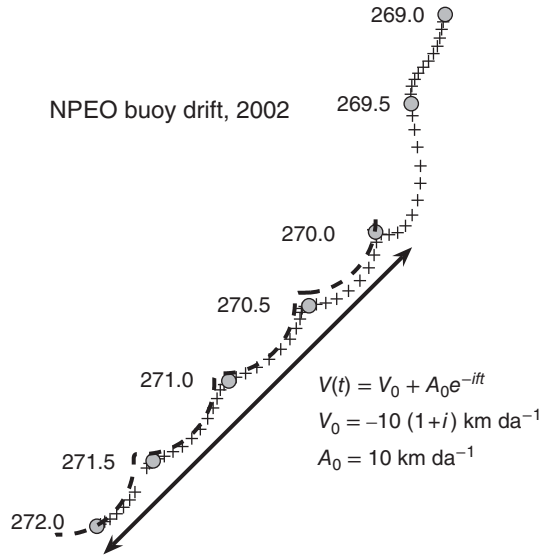$$(i/\omega)\,[D_{cw}(e^{-i\omega t} - 1) + D_{ccw}(1 - e^{i\omega t})] \qquad (5.11)$$

Figure 5.3 Track of an unmanned buoy from 26 to 29 September 2002. + symbols indicate satellite navigation positions every half hour. The dashed curve is the integral of the simple velocity expression from the initial position at time 270.0.

where ω is the diurnal tidal frequency. The coefficients are determined by least-squares error minimization from position fixes over a time comparable to the longest period. An example, calculated by differentiating equation (5.11) evaluated from SHEBA GPS positions every 3 h, is shown in Figure 5.4. Note that V_0 is an estimate of the 'mean' velocity with inertial and tidal components removed. As the upper ocean typically oscillates in phase with the ice, V_0 is often a better indicator of shear, hence turbulence, in the upper part of the boundary layer than is the total ice velocity. With frequent, accurate navigation fixes, other methods provide good velocity estimates, but the main advantage of complex demodulation is that it recognizes the inherent inertia of the rotating ice/IOBL system, and provides a means of rationally separating inertial and tidal motions from the velocity due to shear in the IOBL.

5.2.4 Turbulence scales and eddy viscosity

The simplest approach to describing and modelling turbulent transport perpendicular to mean flow in boundary layer shear flows is by relating flux of a quantity directly to its mean gradient using a proportionality factor with units length squared over time, suggesting that
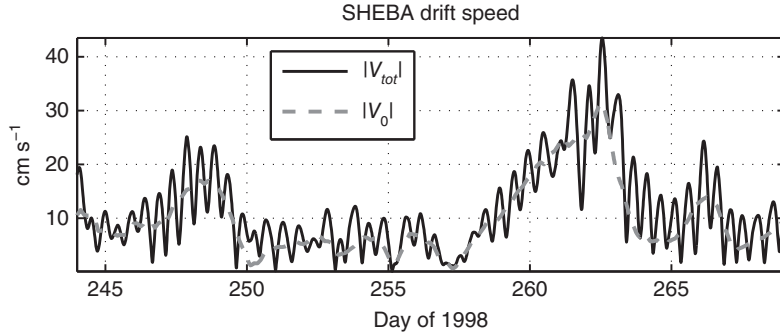
SHEBA drift speed

Figure 5.4 Surface Heat Budget of the Arctic (SHEBA) project station drift speed in September 1998. The dashed curve is the 'mean' velocity after removal of inertial and diurnal tidal components via complex demodulation.

the factor (eddy viscosity if the property is momentum flux, and eddy diffusivity for scalar fluxes) is the product of turbulent velocity and length scales, e.g. kinematic stress:

$$\langle w' \boldsymbol{u}' \rangle = -K\boldsymbol{u}_z = -u_\tau \lambda \boldsymbol{u}_z \qquad (5.12)$$

where $\boldsymbol{u}_z = \partial \boldsymbol{u}/\partial z$ is shear, u_τ is a turbulent velocity scale, and λ is a length scale expressing the vertical displacement over which the turbulent eddies are effective at exchanging momentum (not necessarily the actual vertical excursion of fluid in the eddies). A major thrust of IOBL turbulence measurements over the past three decades has been aimed at elucidating what controls these scales.

5.2.5 Neutral stratification

The IOBL that forms when there is shear between the ice and underlying ocean is often relatively unaffected by changes in density, when melting or freezing is slow, and when the upper ocean is well mixed in both temperature and salinity to reasonably large depths. These so-called neutral boundary layers (meaning that gravitational forces are negligible compared with friction arising from inertial forces in the fluid) provide a good starting point for considering the general problem of ice–ocean exchange.

It is well established that in the lower tens of metres of the neutral boundary layer of the atmosphere, (i) turbulent stress is relatively constant, equal to boundary stress; (ii) stress and velocity are nearly aligned; and (iii) the velocity profile follows the 'law of the wall':

$$\boldsymbol{u}(z) = \frac{\boldsymbol{u}_{*_0}}{\kappa} \log \frac{z}{z_0} \qquad (5.13)$$

where $\boldsymbol{u}_{*_0}$ is friction velocity, a vector defined in terms of the vector kinematic boundary stress, $u_{*_0} \boldsymbol{u}_{*_0} = \boldsymbol{\tau}_0$; z_0 is the hydraulic roughness of the boundary, typically about 1/30th the size of roughness elements on the surface; and κ is von Kàrmàn's constant, ~0.4. An obvious choice of turbulent velocity scale is u_{*_0}, so applying these stipulations to equation (5.12) with $u_z = u_{*_0}/(\kappa z)$, it follows from equation (5.13) that $\lambda = \kappa z$ in the region of the flow where (i)–(iii) hold, by convention called the surface layer. In terms of dimensional analysis, this implies that shear is a function of only two independent variables, u_{*_0} and z, with independent dimensions, hence by the Pi theorem (e.g. Barenblatt, 1996), a dimensionless group formed from u_z, z, and u_{*_0} is a constant (equal to $1/k$), and:

$$\phi_m = \frac{\kappa z u_z}{u_{*_0}} = 1 \qquad (5.14)$$

In atmospheric terminology, ϕ_m is the dimensionless wind shear in the surface layer.

The surface layer approximation assumes rotation (Coriolis force) is unimportant in formulating the relation between shear and stress. However, from the perspective of the Ekman approach, i.e. that eddy viscosity is invariant with depth, the outer part of the boundary layer behaves quite differently from the surface layer, a view corroborated by measurements like those shown in Figures 5.1 and 5.2 where rotational effects are obvious. If we assume that away from the surface layer, shear depends on f as well as u_{*0} and z, then dimensional analysis leads to

$$\frac{z u_z}{u_{*_0}} = \Phi\left(\frac{fz}{u_{*_0}}\right) = \Phi(\xi) \qquad (5.15)$$

introducing the planetary scale, u_{*_0}/f. For the IOBL, with moderate stress ($u_{*_0} = 0.01$ m s^{-1}), the planetary scale is ~70 m at high latitudes. When sea ice moves in a state of free drift (internal stress gradients negligible in the force balance), IOBL boundary stress is usually comparable to wind stress. The ratio of friction velocities then equals the inverse square root of the density ratio, and hence the planetary scale in the atmosphere is roughly 30 times that of the IOBL. This large disparity between the respective boundary-layer scales demonstrates why IOBL measurements are almost always made either beyond the surface layer or at its outer fringes (i.e. IOBL measurements at 2 m would correspond to atmospheric measurements atop a 60 m tower).

A simple way of reconciling the surface and outer layers is to assume that when $\xi = z/(u_{*_0}/f)$ is small (i.e. in the surface layer), λ is governed by the geometric scale, kz, but that in the outer layer, eddies no longer sense their distance from the boundary, and λ is governed instead by some small fraction of the planetary scale, $\Lambda_* u_{*_0}/f$. An extensive series of measurements in the neutrally stratified IOBL has reinforced this theme (McPhee, 1994, 2008b; McPhee & Smith, 1976; McPhee & Martinson, 1994). An approximate value emerging from these studies for the similarity parameter Λ_* is 0.028, which for a typical planetary scale implies that mixing length in the outer layer is about 2 m.

A practical result from comparisons between directly measured stress in the IOBL and variance (energy) wavenumber spectra of the vertical velocity component has been the emergence of a close inverse relationship between λ and wavenumber, k_{max}, at the peak in the area-preserving w spectrum (McPhee & Smith, 1976; McPhee & Martinson, 1994): $\lambda = c_\lambda/k_{max}$, with $c_\lambda \approx 0.85$. With this relationship, it is then possible to estimate the local eddy viscosity:

$$K_{local} = c_\lambda u_*/k_{max}$$

where u_* is obtained either from direct covariance estimates of Reynolds stress or from the w spectrum itself (e.g.McPhee, 2004). With the latter, measuring just vertical velocity spectra at particular levels provides estimates of eddy viscosity. McPhee and Martinson (1994) showed that discrete-level estimates made by this method agreed reasonably well with a bulk estimate of eddy viscosity from an exponential fit of measured Reynolds stress, and with an estimate of thermal eddy

diffusivity obtained by dividing average upward heat flux by the negative temperature gradient.

Another application of using the 'measured' mixing length to infer important characteristics of IOBL scales comes from the ISPOL experiment in the western Weddell Sea in 2004–2005 (McPhee, 2008a). Turbulence was measured at several levels, providing covariance estimates of $u_{*(cov)} = |\langle u'w'\rangle + i\langle v'w'\rangle|^{1/2}$ and $\lambda = 0.85/k_{max}$ from averaged w spectra versus $u_{*(cov)}$ (Figure 5.5); we can gauge to what degree the turbulence scales are controlled dynamically by the planetary ($\Lambda_* u_{*_0}/f$) scaling as opposed to the geometric limit of distance from the boundary. Despite typically large scatter in the turbulence data, a least-squares fit through the origin indicates that λ is often controlled by rotation, and is on average relatively predictable.

If λ scales with u_{*_0}/f through most of the IOBL beyond a thin surface layer, the average eddy viscosity is $\overline{K} = \overline{u}_* \lambda_{max} \approx \Lambda_* u_{*_0}^2/(\sqrt{2}f)$, as stress varies roughly linearly from its surface value to zero near the base of the IOBL. Thus the non-dimensional mean eddy viscosity is:

$$K_* = f\ \overline{K}/u_{*_0}^2 \approx 0.02$$

consistent with various estimates from IOBL data (e.g. McPhee & Martinson, 1994). Note that it is also consistent with Ekman's (1905) assertion that eddy viscosity in the ocean varied with the square of the wind speed.
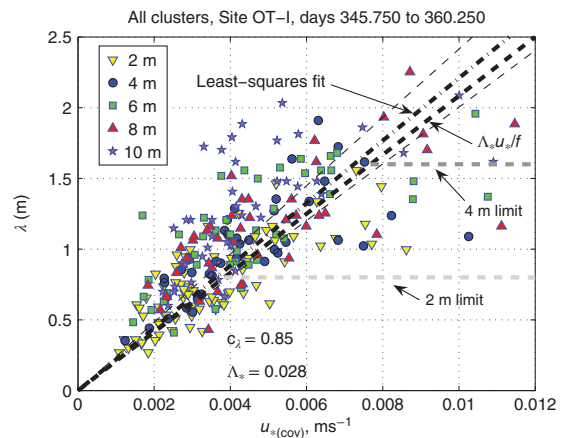

All clusters, Site OT–I, days 345.750 to 360.250

Figure 5.5 Mixing length as inferred from k_{max} (from vertical velocity spectra) versus $\boldsymbol{u}_*$ from 3 hour average turbulence statistics and spectra. The dot-dashed line is a least-squares regression through the origin with 95% confidence interval indicated by light dashed lines. The heavy dashed line indicates the dynamic (planetary) maximum mixing length. Grey dashed horizontals indicate geometric (kz) limits at 2 and 4 m.

5.2.6 Buoyancy impact on turbulence scales

Ice melting or freezing modifies IOBL turbulence in much the same way that nocturnal surface cooling or diurnal heating either quells or enhances turbulence in the atmospheric boundary layer. When ice is melting, turbulent eddies must work against gravity to transport momentum and scalar properties downward, and consequently, for the same stress, the turbulence scales are suppressed and exchange is limited to depths smaller than would be expected under neutral conditions. By the same token, freezing enhances turbulence scales by converting potential energy of the water column to turbulent energy. These tendencies are quantified by considering a third length scale, introduced by Obukhov (1971, English translation):

$$L_0 = \frac{u_{*_0}^{\,3}}{\kappa \langle w'b' \rangle_0} \qquad (5.16)$$

L_0 is positive when ice is melting, as salinity flux is upward, and negative for freezing. Atmospheric boundary-layer studies have established that non-dimensional shear and analogous scalar gradients across the surface layer follow Monin–Obukhov similarity, i.e.:

$$\frac{z u_z}{u_{*_0}} = \phi_m(\zeta); \quad \zeta = z/L_0 \qquad [\text{surface layer}] \quad (5.17)$$

In the surface layer, $\lambda_{sl} = \kappa z/\phi_m$. The form of the similarity parameter ϕ_m has been extensively studied for the atmospheric surface layer, resulting in a variety of empirical functions (Businger et al., 1971; Lettau, 1979). The impact of small positive ζ (stabilizing) is to decrease λ_{sl} and increase shear, while the opposite holds for ζ small and negative (destabilizing).

By comparison with the atmospheric surface layer, there is a paucity of data on the impact of boundary buoyancy flux on the IOBL. However, measurements of turbulence during rapid melting (McPhee et al., 1987; Sirevaag, 2009) and at the edges of freezing leads (McPhee, 1994; McPhee & Stanton, 1996) have provided an important insight into how buoyancy affects turbulence, including in the region beyond the surface layer. For the IOBL stably stratified by surface buoyancy flux (melting), a similarity theory incorporating the three scales discussed so far adequately describes how positive buoyancy flux influences IOBL scales (McPhee,

1981, 1994, 2008b). In that approach the scales for the outer layer are:

$$
\begin{aligned}
\text{Length}: & \quad \eta_* u_{*_0}/f \\
\text{Velocity}: & \quad \boldsymbol{u}_{*_0}/\eta_* \\
\text{Eddy viscosity}: & \quad (u_{*_0}\eta_*)^2/f \\
\text{Kinematic stress}: & \quad u_{*0}\boldsymbol{u}_{*_0}
\end{aligned}
$$

$$\eta_* = \left(1 + \frac{\Lambda_* \mu_*}{\kappa R_c} \right)^{-1/2} \qquad (5.18)$$

where $\mu_* = u_{*_0}/(f L_0)$ is the ratio of the planetary scale to the Obukhov length, R_c is the critical flux Richardson number (~ 0.2), and $\boldsymbol{u}_{*_0}$ is vector (complex) friction velocity. The stability parameter η_* represents a harmonic mean for the maximum mixing length in the outer layer that asymptotically approaches the following limits:

$$
\begin{aligned}
\lambda_{\max} &\to \Lambda_* u_{*_0}/f \quad \text{for } L \to \infty \\
\lambda_{\max} &\to R_c \kappa L \qquad \text{for } L \to 0^+
\end{aligned} \qquad (5.19)
$$

so that:

$$\lambda_{\max} = \eta_*^{\,2} \Lambda_* u_{*_0}/f \qquad (5.20)$$

Stabilizing buoyancy flux ($\eta_* < 1$), is a sink for turbulent kinetic energy, and thus shear is required for turbulence. However, destabilizing buoyancy flux (e.g. from rapid freezing) is a turbulent kinetic energy source, and it is possible to have significant turbulence with little or no ice–ocean shear. In that case, dimensional analysis suggests that the scale velocity in pure free convection ought to be proportional to the cube root of a scale velocity multiplied by the buoyancy flux magnitude. A more common condition is mixed forcing where both density driven convection and shear contribute to turbulence. Again, from dimensional analysis and considering asymptotic behaviour, a workable expression for the scale velocity under these conditions is:

$$w_* = (u_*^{\,3} - \lambda_{\max} \langle w'b' \rangle)^{1/3}; \quad \langle w'b' \rangle < 0 \quad (5.21)$$

When L is negative, $\eta_* > 1$, and according to equation (5.20), $\lambda_{\max}$ increases rapidly. A practical limit on the vertical extent of turbulent eddies is the depth of the well-mixed layer (WML), so we posit that $\lambda_{\max}$ expands until it reaches a limiting value that is some fraction ($0.2 \le c_{ml} \le 0.4$) of the depth of the WML, i.e. $\lambda_{\max} \le c_{ml}|z_{pyc}|$. This allows mixing length to smoothly transition between neutral and unstable scaling.

5.2.7 Rossby similarity

A problem that often arises in considering ice–ocean interaction is how stress at the interface is related to ice velocity (considered with respect to undisturbed geostrophic current). While this is often described by a drag coefficient (e.g. $\tau_0 = c_D V_0^2$), it is convenient in the context of ice–ocean interaction to consider instead a non-dimensional fluid velocity formed by dividing complex surface velocity by vector $\boldsymbol{u}_{*_0}$. The non-dimensional velocity is in effect an inverse square root of the drag coefficient:

$$U_0 = V_0 / u_{*_0} = 1/\sqrt{c_D} \qquad (5.22)$$

As an example, if $\boldsymbol{V}_0$ were the velocity of the ice relative to a level, $z = -2\,\text{m}$, within the surface layer governed by the law of the wall (equation 5.13), the non-dimensional velocity would be:

$$U_0 = \frac{1}{\kappa} \log \frac{2}{z_0} = \frac{1}{\sqrt{c_h}}$$

In this case U_0 is real, as $\boldsymbol{V}_0$ and $\boldsymbol{u}_{*_0}$ are assumed to be aligned (in reality, at the far extent of the surface layer, they generally are not). A typical undersurface roughness for multi-year pack ice is about 0.04 m, for which $U_0 = 9.8$ and $c_2 = 0.0105$.

Although it is common practice to express ocean drag on ice as proportional to the square of velocity relative to the current at the far extent of the IOBL (e.g. the geostrophic current) with a constant turning angle (Hibler, 1979), there are several drawbacks to a quadratic drag approach, particularly in light of recent rapid change in the character of the Arctic ice pack (McPhee, 2012). Starting from the premise that surface velocity depends on variables f, u_{*_0}, and z_0, two with independent dimensions, elementary dimensional analysis suggests that non-dimensional surface velocity should be a function of the ratio of the planetary scale to surface roughness:

$$\frac{\boldsymbol{V}_0}{\boldsymbol{u}_{*_0}} = U_0 \left(\frac{u_{*_0}}{fz_0} \right) \qquad (5.23)$$

Note that equation (5.23) is a quadratic drag expression only if its right-hand side is constant. The interplay between hydraulic roughness and the planetary scale is illustrated in Figure 5.6. Figure 5.6(a) shows measurements from the 1972 AIDJEX IOBL currents (see Figure 5.1). The vector labelled $\boldsymbol{V}_E$ corresponds to the
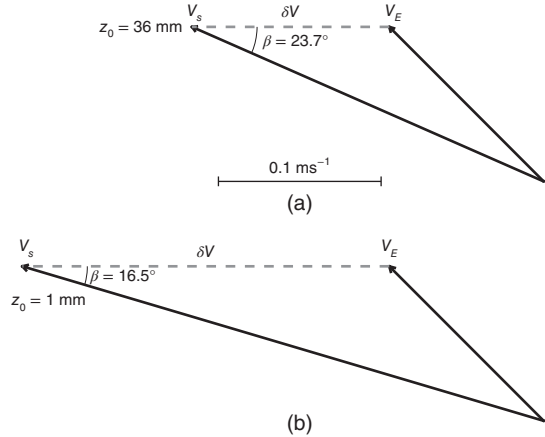

Figure 5.6 (a) Estimating undersurface hydraulic roughness from the Arctic Ice Dynamics Joint Experiment (AIDJEX) measurements (Figure 5.1), assuming the shear between the $\boldsymbol{V}_E$ and $\boldsymbol{V}_s$ follows the law of the wall. (b) For the same Ekman velocity and planetary scale, a smoother surface results in higher surface speed and reduced Coriolis turning.

velocity (relative to the base of the IOBL) at the upper limit of the Ekman layer. We estimated that friction speed during this time was $u_{*_0} = 0.01$ m s^{-1}. The near surface velocity field was distorted by local under-ice morphology (McPhee & Smith, 1976), but as the ice moved as a unit over the entire area observable from the ice station, total shear represented integration over a much larger area than in the immediate vicinity of the instrument mast. If the vector velocity difference $\delta V = V_s - V_E$ is the shear across the logarithmic surface layer, the inferred larger-scale roughness is about 0.04 m. In Figure 5.6(b), we consider an Ekman layer with the same planetary scale, u_{*_0}/f, but much smaller roughness length, $z_0 = 1$ mm , typical of first-year ice in the Weddell Sea (McPhee et al., 1999). The shear across the surface layer is increased, and for the same stress, ice moves about 40% faster, 7° closer to the surface stress direction.

The non-dimensional ice velocity has a direct analogue in the relationship between atmospheric geostrophic wind (proportional to the gradient of the surface pressure field) and wind stress at the surface. From the same principles as discussed qualitatively above, asymptotically matching surface and outer layers (Rossby & Montgomery, 1935; Blackadar & Tennekes, 1968) leads to a functional form for U_0 (representing either the non-dimensional geostrophic wind or ice

velocity relative to the undisturbed ocean). In complex notation, Rossby similarity drag is:

$$U_0 = \frac{1}{\kappa}(\log\ Ro_* - A \mp iB) \qquad (5.24)$$

where $Ro_* = u_{*_0}/(fz_0)$ is the surface friction Rossby number. The sign of the imaginary part depends on the hemisphere (northern negative for the IOBL). The similarity constants, A and B, may be obtained empirically from measurements or derived analytically from similarity scaling principles (McPhee, 1990; 2008b). Typical estimated values from IOBL studies are $A = 2.3$ and $B = 2.1$, but these are subject to a fair amount of variability because other factors, including the impact of boundary buoyancy flux, surface inhomogeneity or relatively shallow mixed layers, are often present and unaccounted for in the simple similarity approach.

The right-hand side of equation (5.24) depends on the planetary scale, so that for a given surface roughness, the drag coefficient varies with surface stress. In similarity terms, the non-dimensional surface roughness, fz_0/u_{*_0}, decreases with increasing stress (i.e. the surface appears smoother), so that the drag coefficient and turning angle also decrease (Figure 5.7). At higher ice speeds, this can represent a significant reduction in drag over what would be expected if the relationship between stress and velocity were quadratic (constant drag coefficient).

When ice melts rapidly, as it often does when blown across temperature fronts existing in the marginal ice zone, the surface buoyancy flux reduces turbulence scales and, in effect, reduces the frictional coupling between the IOBL and the underlying ocean. From dimensional analysis, this adds a second dimensionless parameter, the ratio of planetary to Obukhov lengths, to equation (5.23):

$$U_0 = U_0\left(\frac{u_{*_0}}{fz_0},\ \frac{u_{*_0}}{fL_0}\right) = U_0\ (Ro_*,\ \mu_*)$$

Consistent application of the similarity scaling equation leads to:

$$U_0 \simeq -i\delta(1 + \delta\xi_{sl}) + \frac{\eta_*}{\kappa}\left[\log\frac{\xi_{sl}}{\xi_0} - (a - \delta)\xi_{sl} - \frac{a\delta}{2}\xi_{sl}^2\right] \qquad (5.25)$$

where $\delta = (\pm i/\Lambda_*)$, $a = \frac{\kappa(1-\eta_*)}{\eta_*\Lambda_*}$, and $\xi_{sl} = -\Lambda_*/\kappa$ (McPhee, 1981, 2008b). Manipulation of equation (5.25) then results in a modified Rossby similarity expression

$$U_0 = \frac{1}{\kappa}[\log\ Ro_* - A(\mu_*) \mp iB(\mu_*)] \qquad (5.26)$$

Drag reduction from rapid melting may account for the separation of distinct ice edge bands that form when wind pushes ice across the marginal ice zone into relatively warm water (McPhee, 1981, 2012; Mellor et al., 1986). Bands separate from the pack because water in the WML is rapidly cooled by passage of the melting ice and hence presents less 'grease' for ice following the initial vanguard.

5.2.8 Discussion

The interaction of sea ice with the IOBL requires keeping track of fluxes into and out of the IOBL as well as the ice column, and for useful applications requires coupled numerical modelling. Several approaches exist for modelling the IOBL. 'Slab' models consider properties uniform in a (literally) mixed layer, and exchanges at its base depend on bulk properties (including velocity). Examples for the open ocean include Pollard et al. (1973), Niiler and Kraus (1977), Price et al. (1986) and, for the IOBL, Toole et al. (2010). Second moment turbulence closure models (Mellor & Yamada, 1982; Burchard & Baumert, 1995) solve conservation equations on a vertical grid, including separate conservation equations for turbulence kinetic energy and master turbulent length. At a higher level of complexity, large-eddy simulation (LES) models parameterize only sub-grid-scale processes in fully three-dimensional simulations of the equations of motion (Skyllingstad et al., 2003; Harcourt, 2005). LES models require comparatively fine grids and are computationally expensive.

First-order closure models, which provide a computational compromise between the slab models and more complex closure schemes, express turbulent fluxes of momentum and scalar properties directly in terms of the vertical property gradients. In an approach based on IOBL measurements, called local turbulence closure (McPhee, 2008b, chapters 6–8), eddy viscosity in the bulk of the IOBL (where property gradients are small) is the product of the local friction speed (square root of the Reynolds stress) and a mixing length, which in turn depends on surface flux conditions, f, and, within the surface layer, distance from the boundary. Its formulation depends on limiting asymptotic scales identified in equation (5.19). In the fully turbulent flow of the WML (where scalar gradients are small, but not generally zero), we often assume scalar eddy diffusivity is the same as eddy viscosity (Reynolds analogy). In the pycnocline (usually defined as beginning at the depth
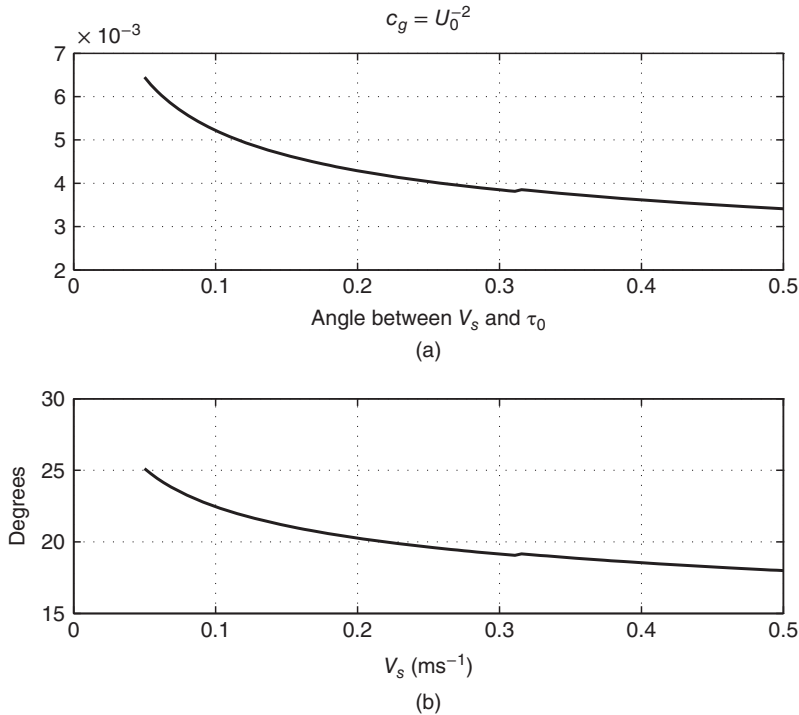
$$c_g = U_0^{-2}$$

(a)

(b)

Figure 5.7 Drag coefficients from Rossby similarity with $A = 2.3$, $B = 2.1$, and $z_0 = 0.03$ m. (a) Effective drag coefficient. (b) Amplitude of the turning angle.

where buoyancy frequency exceeds a given threshold), the algorithm for λ is like the WML formulation, but is based on fluxes computed at the top of the pycnocline. When the density gradient is stabilizing, eddy diffusivity is reduced from eddy viscosity following a formula based on local Richardson number, derived from laboratory measurements reported by Turner (1973). The basic mixing length parameterization is illustrated if Figure 5.8. Note the gradients in density drawn in the WML for stable (Figure 5.8b) and statically unstable (Figure 5.8c) cases. When we measure scalar fluxes in the IOBL, we invariably see finite, albeit small, mean scalar gradients.

A key element for the IOBL is z_0, the hydraulic roughness of the ice undersurface. Estimates vary widely depending on ice age, location and the amount of local deformation (e.g. Shirasawa, 1986, table 3; McPhee, 1990, table 6.1). For undeformed, first-year year ice grown in place (Svalbard fjords, Canadian Arctic Archipelago), the undersurface is often found to be hydraulically smooth (Langleben, 1982; McPhee

et al., 2008; Crawford et al., 1999). Surface roughness for first-year ice in the eastern Weddell Sea was estimated to be about 1 mm (McPhee et al., 1999). For the 11-month SHEBA deployment (1997–1998), a local value of z_0 for undeformed, multi-year ice was found to be 6 mm (McPhee, 2002). The method specifically excluded the effects of pressure ridge keels and refrozen leads.

In multi-year pack ice, IOBL measurements are typically made in relatively smooth locations away from obvious obstacles and thus may tend to systematically underestimate the overall roughness of a large floe or regional area representative of a model grid cell. We estimated a regional value for z_0 in multi-year ice in the western Weddell Sea of about 4 cm, using a method that compares modelled angular shear in the outer part of the IOBL with observed results over relatively long averaging periods (McPhee, 2008a). The method applied to the SHEBA data set yielded a similar value, 4.9 cm (McPhee, 2008b), and a value of about 9 cm for rough ice surrounding a buoy deployed near the North Pole (Shaw
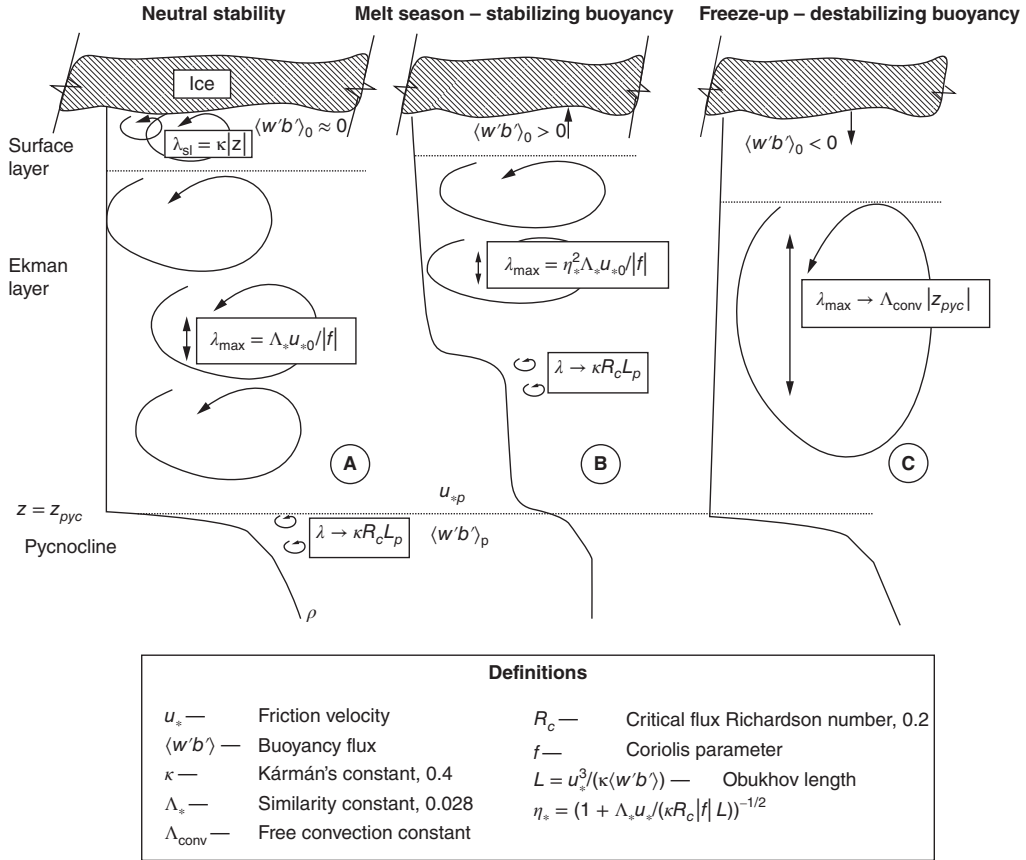
Neutral stability   **Melt season – stabilizing buoyancy**   **Freeze-up – destabilizing buoyancy**

Ice

$\lambda_{sl} = \kappa |z|$ $\langle w'b' \rangle_0 \approx 0$ $\langle w'b' \rangle_0 > 0$ $\langle w'b' \rangle_0 < 0$

Surface layer

Ekman layer

$\lambda_{max} = \eta_*^2 \Lambda_* u_{*0}/|f|$

$\lambda_{max} = \Lambda_* u_{*0}/|f|$ $\lambda_{max} \rightarrow \Lambda_{conv}|z_{pyc}|$

$\lambda \rightarrow \kappa R_c L_p$

A   B   C

u_{*p}

$z = z_{pyc}$ $\lambda \rightarrow \kappa R_c L_p$ $\langle w'b' \rangle_p$

Pycnocline

ρ

Definitions

u_* —	Friction velocity	R_c —	Critical flux Richardson number, 0.2
$\langle w'b' \rangle$ —	Buoyancy flux	f —	Coriolis parameter
κ —	Kármán's constant, 0.4	$L = u_*^3/(\kappa \langle w'b' \rangle)$ —	Obukhov length
Λ_* —	Similarity constant, 0.028	$\eta_* = (1 + \Lambda_* u_*/(\kappa R_c |f| L))^{-1/2}$	
Λ_{conv} —	Free convection constant		

Figure 5.8 Mixing length representation under different conditions of surface buoyancy flux: (a) neutral, (b) stable, and (c) statically unstable.

et al., 2008). The latter is comparable to estimates from the marginal ice zone (Johannessen, 1970; Pease et al., 1983). Lu et al. (2011) described an alternate method for parameterizing sea ice drag by partitioning it among bottom skin friction and form drag on pressure ridge keels and floe edges.

It is useful to recall that it is log z_0 that appears in the equations, not the actual length. Even so, the range is quite large. While the scatter in z_0 estimates makes categorization risky, in lieu of better information a rough guide might be to assign the following values: for undeformed fast ice, $z_{0s} = (\nu/u_{*_0})e^{-2}$ (hydraulically smooth); for first-year sea ice, ~ 1 mm; for typical multi-year pack ice, 5 cm; for highly deformed pack ice, ~10 cm (McPhee, 2012).

5.3   The ice–ocean interface

5.3.1   Enthalpy and salt balance at the interface

In an idealized control volume following the interface (Figure 5.9), three terms dominate the heat equation, which may be written in 'kinematic' form (i.e. after dividing by ρc_p, the product density and specific heat of seawater) as

$$-\dot{q} + \langle w'T' \rangle_0 = w_0 Q_L \qquad (5.27)$$

where $\dot{q} = -K_{ice} T_z/(\rho c_p)$ represents heat conduction in the ice column with thermal conductivity K_{ice} and temperature gradient T_z; $\langle w'T' \rangle_0$ is kinematic heat flux from the ocean; $Q_L = L_{ice}/c_p$ is the latent heat of sea ice divided by specific heat (with temperature units); and w_0 is vertical velocity of the interface due to melting or freezing

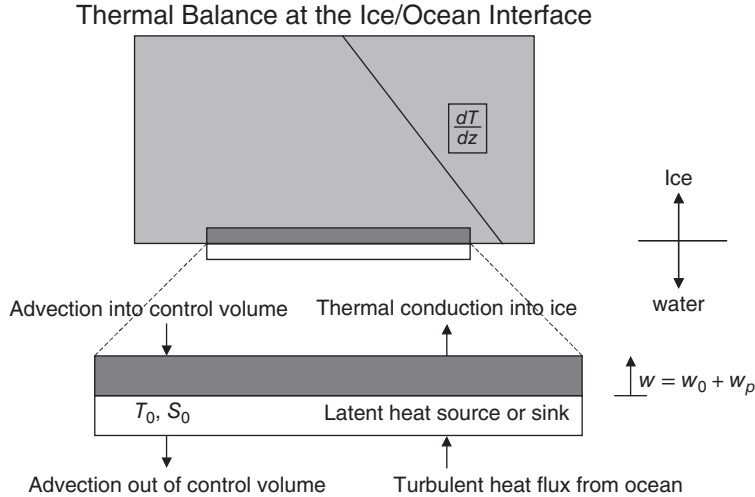## Thermal Balance at the Ice/Ocean Interface

Figure 5.9 Simplified schematic of the heat balance at the ice–ocean interface, with control volume following the boundary.

(i.e. the isostatically balanced basal melt rate). Advective flux associated with w_0 is neglected, assuming that temperatures of fluid entering and leaving the control volume are nearly the same. Thermal properties of sea ice are functions of brine volume and temperature (Notz & Worster, 2009). Here we use simplified expressions for thermal conductivity from Untersteiner (1961):

$$K_{ice} \approx K_{fresh} + \beta S_{ice}/T_{ice}$$

where K_{fresh} is 2.04 J m^{-1} K^{-1} s^{-1} and $\beta = 0.117$ J K^{-1} s^{-1} psu^{-1} °C, and for latent heat from Maykut (1985):

$$Q_L = \frac{L_{fresh}}{c_p}(1 - 0.03S_{ice})$$

When sea ice melts, the interface is typically very smooth and hard, and turbulent flux of salt ($\langle w'S'\rangle_0$) into the control volume is balanced mainly by an advective flux given by w times the difference between the salinity of water at the interface and ice salinity:

$$\langle w'S'\rangle_0 + w(S_{ice} - S_0) = 0 \qquad (5.28)$$

For generality, the vertical interface velocity, $w = w_0 + w_p$, includes a second term, w_p, intended to incorporate the idea that a percolation flow of fresh or brackish water driven by a pressure head in the ice column could induce upward interface motion (and negative salinity flux) without direct melting. In most applications and it what follows, w_p is ignored.

When ice freezes, there is substantial evidence that the simple balance expressed by equation (5.28) does not adequately account for the salt transfer in an infinitesimal control volume following the interface. The leading edge of growing sea ice appears to be a combination of crystalline ice and entrapped liquid brine in a so-called mushy layer (Wettlaufer et al., 1997; Feltham et al., 2006), and that near the growing interface, S_{ice} approaches the salinity of the melt (Notz & Worster, 2009); hence the advective flux is small. What this implies for the IOBL boundary condition is discussed below.

5.3.2   Measurements

Instrument clusters, including highly accurate ocean thermometers mounted near three-dimensional arrays of current meters, were deployed in the IOBL during the Marginal Ice Zone Experiment (MIZEX) in 1984, so that in addition to turbulent stress, accurate estimates of turbulent heat flux were available for the first time (McPhee et al., 1987). Near the end of MIZEX, northerly winds pushed our floe south into water where the mixed layer temperature was well above freezing. Measured heat flux and basal melt rate increased substantially, but were still considerably smaller than we had anticipated from previous modelling studies, and when the floe on which we were drifting did not melt away, it was clear that we had to re-examine our treatment.
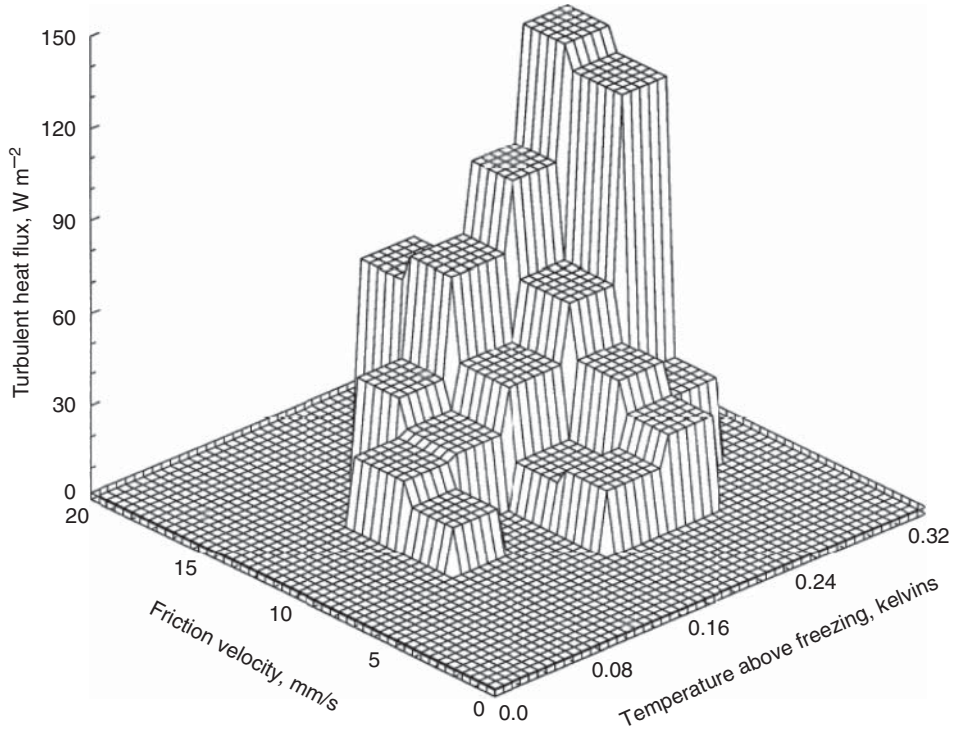
Figure 5.10 Directly measured heat flux averaged in bins of ΔT and $\boldsymbol{u}_*$ for all data from Marginal Ice Zone Experiment (MIZEX) in 1984. Source: Adapted from McPhee, 1992. Reproduced with permission of American Geophysical Union.

Results from the combination of heat flux and Reynolds stress measurements during MIZEX are summarized in Figure 5.10 (McPhee, 1992), intended to illustrate that ocean heat flux depends on both temperature elevation from freezing and friction speed, u_*. MIZEX and subsequent studies suggested a simple empirical parameterization of kinematic heat flux of the form:

$$\frac{H_f}{\rho c_p} = \langle w'T' \rangle_0 = St_* u_{*_0} \Delta T \qquad (5.29)$$

where $\Delta T = T_{ml} - T_f(S_{ml})$ is the elevation of mixed layer temperature above its salinity determined freezing temperature, and St_* is a turbulent Stanton number. IOBL measurements under widely varying conditions of both u_* and ΔT have shown St_* to be relatively invariant. Over the year-long SHEBA experiment its mean value was estimated to be $St_* = 0.0057 \pm 0.0004$ (McPhee, 2008b).

5.3.3 Interface approximations

The first serious efforts at thermodynamic modelling of sea ice indicated that heat flux from the ocean

was important for maintaining a realistic equilibrium ice thickness. Maykut and Untersteiner (1971) found that without a steady basal flux of about 2 W m^{-2}, ice continued to grow to unrealistically large thickness in their thermodynamic ice model. Using a similar model for Southern Ocean sea ice, Parkinson and Washington (1979) required a constant ocean heat flux about an order of magnitude larger to limit ice growth to observed thickness.

Measurements over several decades have shown that the IOBL, even in the central Arctic with perennially high ice concentrations, spends a sizeable fraction of the year at temperatures above its salinity-determined freezing temperature (Figure 5.11). Thus early in the summer (at maximum insolation) a significant fraction of the solar radiation making its way into the ocean is heating the upper water column, rather than melting ice. For example, during June 1998 at the SHEBA station, we estimated that energy expended in heating the mixed layer was roughly equivalent to the total basal heat transfer. Obviously, the albedo feedback effect (heating creates more open water, absorbing
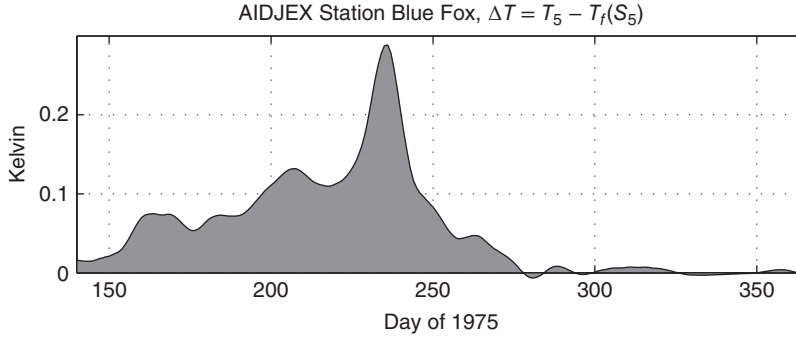
Figure 5.11 Elevation of mixed layer temperature above freezing at the Arctic Ice Dynamics Joint Experiment (AIDJEX) station Blue Fox during the summer of 1975 in the Canadian Basin of the western Arctic.

more solar radiation, opening more water, and so on) is most effective at high sun angles, and the capacity of the upper ocean to absorb heat then and release it to the ice later provides a presumably significant brake on the feedback process.

Critical links in understanding the balances at the interface are the turbulent heat and salinity fluxes. A combination of dimensional analysis and measurements showing little or no Reynolds number dependence for St_* suggests that the following dimensionless expression for the kinematic turbulent heat flux at the interface in terms of a thermal exchange coefficient, α_h, is a function of the Prandtl number:

$$\frac{\langle w'T'\rangle_0}{u_{*_0}\delta T} = \alpha_h\left(\frac{\nu}{\nu_T}\right) = \alpha_h(\mathrm{Pr}) \qquad (5.30)$$

where $\delta T = T_{ml} - T_0$ is the difference in temperature between the far-field fluid and interface (the thermal driving); ν is molecular viscosity; and ν_T is molecular thermal diffusivity. Similarly, we can write a functional expression for dimensionless salinity flux using molecular haline diffusivity, ν_S:

$$\frac{\langle w'S'\rangle_0}{u_{*_0}\delta S} = \alpha_S\left(\frac{\nu}{\nu_S}\right) = \alpha_S(\mathrm{Sc}) \qquad (5.31)$$

where $\delta S = S_{ml} - S_0$ is the difference between far-field and interface salinities, and Sc is the Schmidt number.

5.3.4 The 'two-equation' parameterization
Assuming that water at the interface is at its freezing temperature, $\alpha_h = St_*$ only if salinity there is the same as S_{ml}. For slow melt rates, this is often an adequate approximation, and by calculating $\langle w'T'\rangle_0$ from equation (5.30)

with $\alpha_h = St_*$, an expression for the isostatically adjusted melt rate is:

$$w_0 = \frac{-\dot{q} + St_* u_{*_0}\Delta T}{Q_L} \qquad (5.32)$$

from which salinity flux follows:

$$\langle w'S'\rangle_0 = w_0(S_{ml} - S_{ice}) \qquad (5.33)$$

These may be combined to estimate surface buoyancy flux (an important parameter for the IOBL turbulence):

$$\langle w'b'\rangle_0 = \frac{g}{\rho}\langle w'\rho'\rangle_0 = g(\beta_S\langle w'S'\rangle_0 - \beta_T\langle w'T'\rangle_0) \quad (5.34)$$

where g is the acceleration of gravity, and β_S and β_T are the haline contraction and thermal expansion factors for cold seawater, respectively. For water near freezing β_T is so small that buoyancy flux is controlled almost exclusively by salinity flux, which further simplifies equation 5.34.

5.3.5 The 'three-equation' parameterization
An obvious paradox accompanies the two-equation approach. If there is enough heat flux to initiate melting, salinity of water in the control volume must be less than in the far field, and $\delta T < \Delta T$ so $\alpha_h/St_* = \Delta T/\delta T$, i.e. the thermal exchange factor is larger than St_*. If the Prandtl number is important in the heat transfer process, then it is reasonable to assume that the Schmidt number plays a role in salt transfer. At cold temperatures, the molecular thermal diffusivity is roughly 200 times greater than salt diffusivity, and thus we suspect that if heat and salt exchange depend on Pr and Sc, $\alpha_h \neq \alpha_S$ and the process is inherently 'double-diffusive.'

If water in the control volume is at freezing, the dependence of freezing temperature on salinity, $T_0 = T_f(S_0) \doteq -mS_0$ (where m is the local slope of the freezing curve), may be combined with equations (5.28), (5.30) and (5.31) to obtain a quadratic in, for example, S_0:

$$mS_0^2 + (T_H + T_L - mS_{ice})S_0 - T_H S_{ice} - T_L S_w = 0 \quad (5.35)$$

where

$$T_H = T_{ml} - \frac{\dot{q}}{\alpha_h u_{*_0}}; \qquad T_L = \frac{\alpha_S Q_L}{\alpha_h} \quad (5.36)$$

T_H and T_L are temperature-scale parameters expressing sensible and latent heat forcing, respectively (assuming w_p is negligible as earlier). If α_h and α_S are known, w_0 follows from equation (5.33), providing the melt rate and buoyancy flux.

If heat conduction in the ice column is small, the temperature and salinity at the interface depend on the ratio $R = \alpha_h/\alpha_S = (v_T/v_S)^n$, where the exponent is thought to range from 2/3 to 0.8 based on a combination of laminar theory and empirical results, in turn suggesting a range $35 \le R \le 70$ (Notz et al., 2003). R is a measure of the strength of double diffusion, i.e. as R increases, heat transfer increases relative to salt transfer. For fresh ice with no temperature gradient ($\dot{q} = S_{ice} = 0$), equation (5.35) reduces to

$$S_0 = S_{ml} / \left(1 + {}^{R\delta T} /_{Q_L} \right) \quad (5.37)$$

Q_L is the latent heat of ice divided by specific heat of seawater, about 84 K for fresh ice. In this case if $R = 1$, $Q_L \gg \delta T$, so $S_0 \to S_{ml}$. On the other hand, in water a degree or two above freezing, if R is in the range given above, then $Q_L/R \sim \delta T$ and S_0 may be considerably less than S_{ml}.

5.3.6   Double-diffusion during melting

Most measurements of turbulent heat flux have been made at relatively small values of ΔT: generally from 0.1 to 0.3 K. In areas with low ice concentrations (e.g. in the marginal ice zone) or where ice encounters inflowing warm water (e.g. Whaler's Bay north of Svalbard), ΔT may reach values an order of magnitude or more greater, with much higher melt rates (decimetres day^{-1}) and presumably increased double-diffusive tendency.

When melting depresses salinity at the interface, $\alpha_h/St_* > 1$. For commonly encountered ranges of

stress and thermal forcing ($5 \le u_{*_0} \le 15$ mm s^{-1}; $0.05 \le \Delta T \le 0.5$ K) observed during the field programmes, α_h differs from St_* by less than 2% when $R = 1$ (no double diffusion), while for $R = 70$, it is more than twice as large (McPhee, 2008a, figure 6.6).

The rate-limiting impact of salt diffusion can be examined (Figure 5.12) by considering solutions to equation (5.35) for moderate interface stress ($u_{*_0} = 0.015$m s^{-1}) with bulk thermal driving, ΔT, ranging from 0 (freezing) to 3 K (as might be encountered when ice drifts across a front in the marginal ice zone), and limiting values of R. In the first case with no double diffusion, we specify $R = 1$, $\alpha_h = 0.0058$. For the second, strong double diffusion: $R = 70$, $\alpha_h = 0.0137$. In both cases, the heat exchange coefficient is chosen so that the 'three-equation' solution matches the bulk expression in equation (5.29) (with $St_* = 0.0057$) for small values of ΔT. We emphasize that without direct knowledge of either R or α_h, the main observational constraint is the measured bulk Stanton number. For $R = 1$, the interface thermal driving, δT, (Figure 5.12a, dashed curve) is almost indistinguishable from the bulk driving, i.e. T_0 remains very close to the freezing temperature of the far field. For $R = 70$ (solid curve), δT is much reduced and exhibits positive curvature with increasing ΔT. As might be expected, the saline driving, δS, (Figure 5.12b) is highly dependent on the double-diffusive strength. For $R = 70$, δS approaches 18 psu for large ΔT. For $R = 1$, it remains within about 1 psu of the far field, even with strong thermal forcing. Basal heat flux (Figure 5.12c) follows directly from δT. At high values of ΔT, heat flux for $R = 70$ is half as large again as for $R = 1$. In the latter case, the bulk relation (overlain grey curve in Figure 5.12c) is essentially the same as the three-equation solution.

Because of large temporal and spatial gradients in marginal ice zones, it is notoriously difficult to measure both $\langle w'T' \rangle$ and $\langle w'S' \rangle$ accurately in a rapidly melting environment; however, by careful analysis of turbulence measurements in Whaler's Bay north of Svalbard, Sirevaag (2009) obtained independent estimates of the exchange coefficients: $\alpha_h = 0.0131$ and $\alpha_S = 4 \times 10^{-4}$ with $R \approx 33$ when the average heat flux was 268 W m^{-2}. He also reported a direct bulk Stanton number: $St_* = 0.0084$, which is reasonably close to $(\delta T/\Delta T)\alpha_h = 0.0088$ obtained from reported values. His results thus confirm that heat flux increases with thermal driving in a superlinear fashion, with
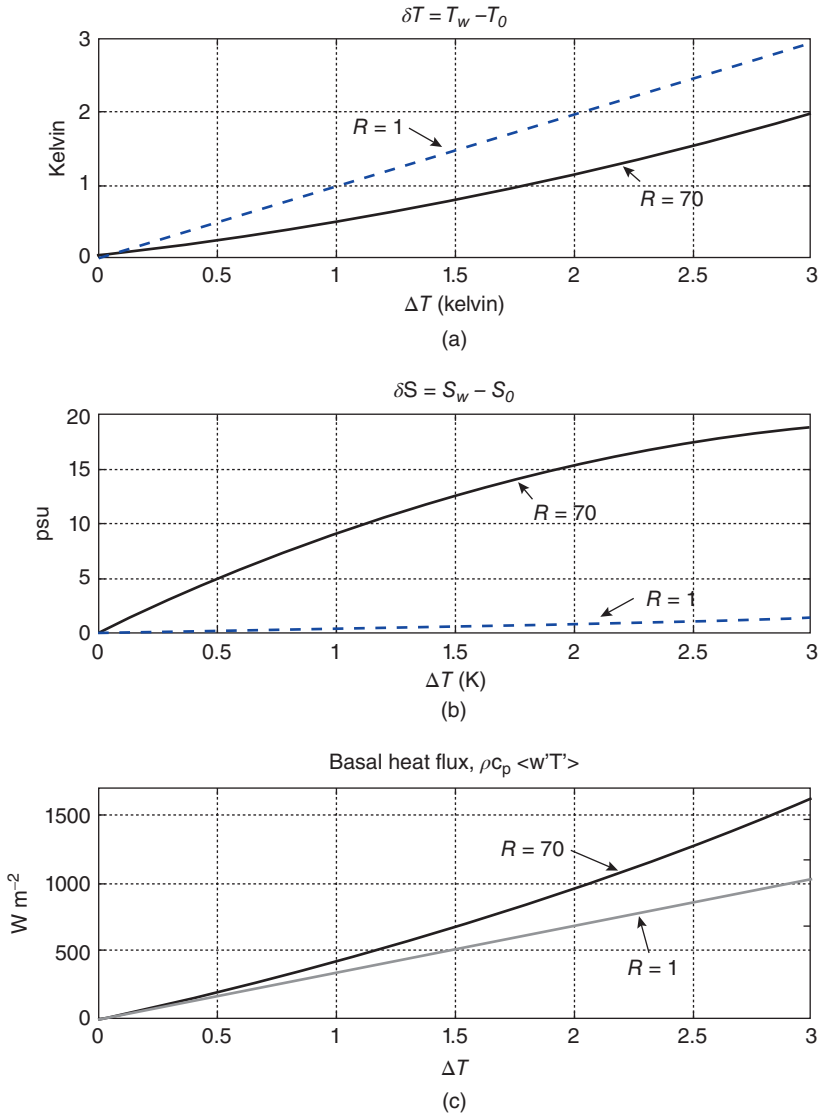
$$\delta T = T_w - T_0$$

$$\Delta T \text{ (kelvin)}$$

(a)

$$\delta S = S_w - S_0$$

$$\Delta T \text{ (K)}$$

(b)

Basal heat flux, $\rho c_p \langle w'T' \rangle$

$$\Delta T$$

(c)

Figure 5.12   (a) $\delta T = T_w - T_0$ versus $\Delta T = T_w - T_f(S_w)$ for $R = 1$, (dashed) and $R = 70$, $\alpha_h = 0.0137$ (solid). Other parameters: $\boldsymbol{u}_{*_0} = 0.015$ m s^{-1}; $S_w = 33$ psu; $S_{ice} = 4$ psu. (b) δS vs ΔT. (c) Basal heat flux versus ΔT. The curve labelled $R = 1$ is overlain in grey by the linear relation: $H_f = \rho c_p St_* \boldsymbol{u}_{*_0} \Delta T$ with $St_* = 0.0057$.

potential importance for estimating ice melt and IOBL stratification in low ice concentration conditions.

5.3.7   False bottoms

Double diffusion also appears to be the controlling factor in the persistence and migration of false bottoms. These occur when concavities in the ice underside fill with fresh meltwater, forming a thin ice layer at the interface between the fresh water and underlying, colder seawater. Observations of the bottom elevation changes at AIDJEX station Big Bear during the summer of 1975 by A. Hanson showed that gauges deployed at the start of summer in relatively thick ice (280–300 cm) indicated relatively continuous bottom melt over the course of the summer, totalling 30–40 cm. In contrast, gauges deployed in thinner ice (160–175 cm) showed

little net bottom melt and even, in some cases, net growth. Hanson attributed this to the formation of so-called false bottoms that occur when concavities in the ice underside fill with fresh meltwater, which then forms a thin layer of ice at the interface with colder seawater. During one 10-day period in August 1975, four of the shallow thickness gauges showed similar changes in bottom elevation, averaging about 15 cm, while the three thick-ice gauges each showed bottom ablation of about 5 cm.

Notz et al. (2003) investigated evolution of false bottoms in both laboratory and natural settings, including a simulation of the AIDJEX event just described. They found that the observed upward migration of the false bottoms could be well simulated with $R = 50$, but that with $R = 1$ (no double diffusion) and observed stress, the initial false bottoms disappeared within a short time. Our experience, particularly at SHEBA, has instead been that they form repeatedly and migrate upwards during the summer, making space for new false bottoms. This produces interleaved layers of ice and fresh water by the time freeze-up begins; numerous examples were observed during the setup for SHEBA in October 1997.

False bottoms may have an important impact on the ice–albedo feedback. First, they shield the thinnest pack ice from direct contact with above-freezing seawater, greatly reducing bottom ablation and reducing the area of low-albedo open water when sun angles are highest. Second, depending on how extensively they cover the ice undersurface, because of the large positive temperature gradient across the fresh ice layer, they act as a source of heat for the upper ocean (Figure 5.13a). The effective bulk Stanton number for ice with area fraction A_{fb} of the undersurface covered by false bottoms or meltwater ponds is:

$$St_{*_{eff}} = H_{total}/(\rho c_p u_{*_0} \Delta T) = \frac{(1 - A_{fb})\langle w'T'\rangle_0 + A_{fb}\langle w'T'\rangle_{fb}}{u_{*_0} \Delta T}$$

As illustrated in Figure 13(b) using results from the double-diffusive false bottom model of Notz et al. (2003), relatively small A_{fb} may significantly decrease the effective heat transfer from the ocean, again lessening the amount of melting when sun angles are high.

5.3.8   Heat and salt exchange during freezing

If the ice–water interface retained its double-diffusive character when ice was forming rather than melting, heat would be extracted from the water column faster than salt was added, and a mixed layer that was initially at freezing would become super-cooled, presumably forming frazil ice. With exchange coefficients appropriate for melting and moderate growth rates, the three-equation formulation indicated significant frazil formation at the same time, slowing direct congelation growth (Mellor et al., 1986; Steele et al., 1989). Holland et al. (1997) considered double-diffusive effects during freezing with a coupled sea ice–ocean numerical model with several ice thickness categories. Frazil accreted equally on all thickness categories with a net increase in heat loss and equilibrium thickness because of more conductive flux through thinner categories.

Observations of multi-year pack ice in the Arctic reveal that neither super-cooling nor frazil production is extensive (Weeks & Ackley, 1986), suggesting that the freezing process was not much affected by double diffusion, at least not to the degree suggested by the models. An experiment designed to test this was conducted in Van Mijenfjorden, Svalbard, in tidal flow under growing fast ice. As reported by McPhee et al. (2008), turbulence data showed an average heat flux of about 1.5 W m^{-2} when upward heat conduction in the ice was estimated to be about 21 W m^{-2}, producing a (downward) salinity flux of about -2×10^{-6} psu m s^{-1}. These data ruled out anything but weak double diffusion, and a more extensive modelling study, using data from the main project and the subsequent student exercises, confirmed that the three-equation interface solution could adequately describe the measured heat flux 1 m below the ice only for $R = 1$.

The IOBL response thus corroborates studies showing that salinity increases rapidly near the base of growing ice (Notz & Worster, 2009) and that the simple advective approach for describing the salt balance at the interface (equation 5.28) is not adequate for growing ice. If equation (5.35) is retained as the governing description, then when ice is freezing, the VMF data and modelling suggest that $R = 1$, which implies that $\langle w'S'\rangle_0 = -\langle w'T'\rangle_0/m$.

An interesting twist on heat transfer at the interface of growing ice was provided by turbulence measurements 1 m beneath fast ice near Erebus Glacier Tongue,
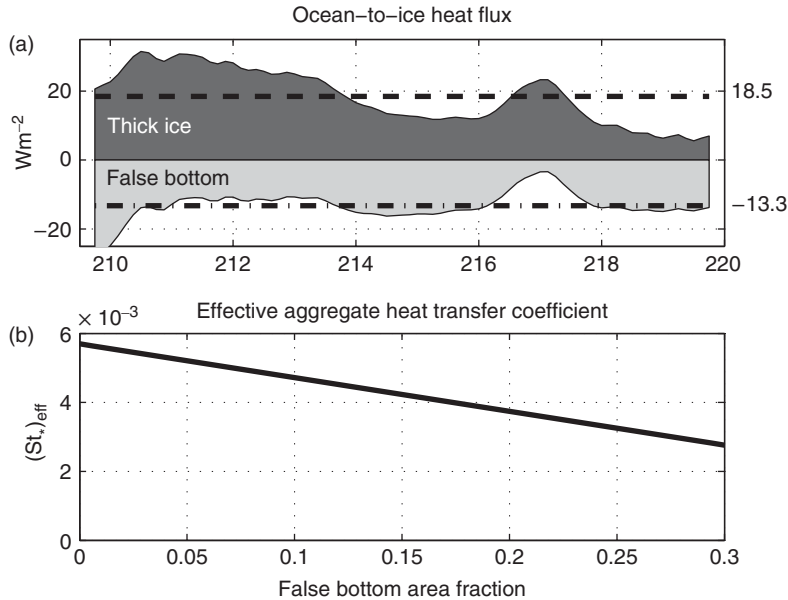
Figure 5.13 (a) Upward heat flux under thick ice (dark shading) and under false bottoms (light shading) from the Arctic Ice Dynamics Joint Experiment (AIDJEX) simulation. Mean values are listed on the right. (b) Corresponding effective bulk Stanton number $(St_*)_{\text{eff}}$ as a function of undersurface false bottom (or melt pond) area coverage.

Antarctica, in October 2010. The upper 35 m of the water column was isothermal such that the top 15 m was super-cooled, i.e. below its pressure-dependent freezing temperature. Super-cooling is often observed near ice shelves debouching into McMurdo Sound as water that has cooled as it circulated under thick ice advects from under the shelf and rises. Although limited in duration by ice accretion on the instrumentation, our results indicated tidally modulated, but consistently downward heat flux (Figure 5.14). Our interpretation is that upward conduction of heat away from the interface in the ice column (~2.3 m thick with 10 cm snow) was insufficient to balance heat released as the super-cooled water finds suitable nucleation sites on the ice undersurface (Robinson et al., 2010). Measured heat flux is shown in Figure 5.14(c) (pentagram symbols with standard deviation error bars), whereas the shaded curve indicates the bulk heat flux, $H_{\text{bulk}} = c_H u_* \Delta T$, where $c_H = 0.01$ is the heat transfer coefficient, and ΔT is the temperature measured 1 m below the ice minus the freezing temperature at 3 dbar. While the record is too short to draw definitive conclusions, the transfer coefficient is similar, if somewhat larger, than $St_{*_{\text{eff}}}$ found for melting. As freezing is adding some negative buoyancy, an increase in the transfer coefficient is not

unexpected. Tidal modulation of the heat flux illustrates the role of shear stress in removing heat from the interface, and suggests that platelet growth on the ice underside may be rate-limited by heat flux into the ocean when conductive flux in the ice column slows.

5.3.9 Discussion

Understanding of thermodynamics and salt transfer at the growing or melting ice–ocean boundary is far from complete. Even the assumption that fluid at the interface is at the liquidus temperature is open to question: Worster (personal communication, 2006) has pointed out that during ice growth, if heat influx outpaces salt loss in fluid draining through brine channels traversing a negative vertical temperature gradient, then it may enter the upper ocean at a temperature slightly above its salinity-determined freezing point.

While recognizing these limitations, McPhee et al. (2008) suggested that a parameterization of boundary fluxes for sea ice in direct contact with the IOBL is as follows: with T_w, S_w, and $\boldsymbol{u}_{*_0}$ specified either from measurements or modelling/parameterization, along with pertinent ice parameters $(S_{ice}, .q)$, solve equation (5.35) with $\alpha_h = 0.0093$ and $R = 35$ (to satisfy the St_* constraint). If the resulting heat balance grows
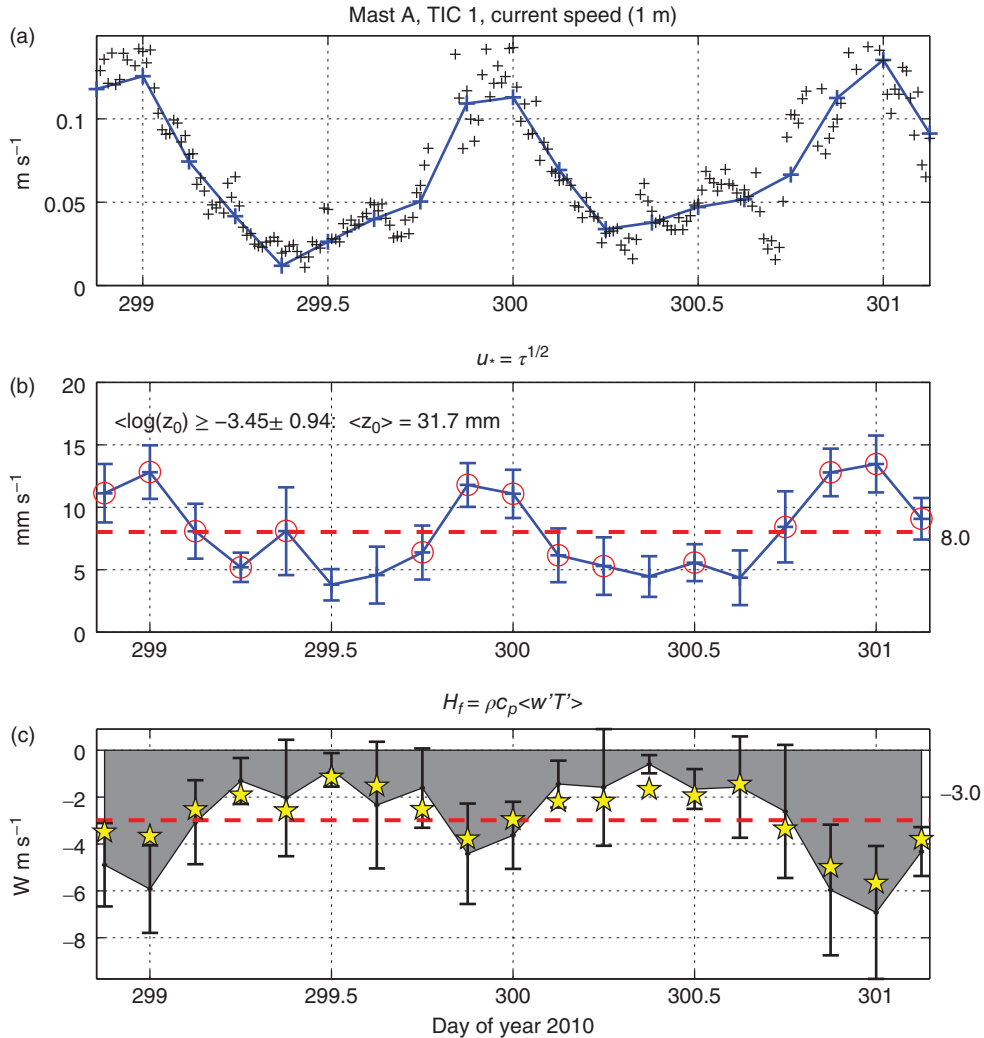
Figure 5.14 Current speed (a), friction speed (b) and turbulent heat flux (c) 1 m below fast ice near Erebus Glacier Tongue, Antarctica. Plus symbols (+) in (a) are current speeds for each 15-minute average used for covariance realizations. For direct flux measurements [circles in (b) and pentagrams in (c)], error bars indicate the standard deviation of 15-minute covariance realizations in each 2-hour average. The shaded curve in (c) is the bulk heat flux relation discussed in the text.

ice, then redo the calculation with $R = 1$ to eliminate double-diffusive effects.

References

Barenblatt, G.I. (1996) *Scaling, Self-similarity and Intermediate Asymptotics*. Cambridge University Press, Cambridge.

Blackadar, A.K. & Tennekes, H. (1968) Asymptotic Similarity in Neutral Barotropic Planetary Boundary Layers. *Journal of the Atmospheric Sciences*, **25**, 1015–1020.

Burchard, H.& Baumert, H. (1995) On the performance of a mixed-layer model based on the k-ε turbulence closure. *Journal of Geophysical Research: Oceans*, **100**(C5), 8523–8540.

Businger, J.A., Wyngaard, J.C., Izumi, Y. & Bradley, E.F. (1971) Flux-profile relationships in the atmospheric surface layer. *Journal of the Atmospheric Sciences*, **28**, 181–189.

Crawford, G., Padman, L. & McPhee, M.G. (1999) Turbulent mixing in Barrow Strait. *Continental Shelf Research*, **19**, 205–245.

Ekman, V.W. (1905) On the influence of the earth's rotation on ocean currents. *Arkiv för Matematik, Astronomi och Fysik*, **2**, 1–52.

Feltham, D.L., Untersteiner, N., Wettlaufer, J.S. & Worster, M.G. (2006) Sea ice is a mushy layer. *Geophysical Research Letters*, **33**, L14501.

Gill, A.E. (1982) *Atmosphere-Ocean Dynamics, XV*. Academic Press, New York.

Harcourt, R.R. (2005) Thermobaric cabbeling over Maud Rise: theory and large eddy simulation. *Progress in Oceanography*, **67**, 186–244.

Hibler, W.D. (1979) A dynamic thermodynamic sea ice model. *Journal of Physical Oceanography*, **9**, 815–846.

Holland, M.M., Curry, J.A. & Schramm J.L. (1997) Modeling the thermodynamics of a sea ice thickness distribution: 2. Sea ice/ocean interactions. *Journal of Geophysical Research: Oceans*, **102**, 23093–23107.

Hunkins, K. (1966) Ekman drift currents in the Arctic Ocean. *Deep Sea Research and Oceanographic Abstracts*, **13**, 607–620.

Johannessen, O.M. (1970) Note on some vertical profiles below ice floes in the Gulf of St. Lawrence and near the North Pole. *Journal of Geophysical Research*, **75**, 2857–2861.

Langleben, M.P. (1982) Water drag coefficient of first-year sea ice. *Journal of Geophysical Research: Oceans*, **87**(C1), 573–578.

Lettau, H. (1979) Wind and temperature profile prediction for diabatic surface layers including strong inversion cases. *Boundary-Layer Meteorology*, **17**, 443–464.

Lu, P., Li, Z., Cheng, B. & Leppäranta M. (2011) A parameterization of the ice-ocean drag coefficient. *Journal of Geophysical Research: Oceans*, **116**, C07019.

Maslanik, J., Stroeve, J., Fowler, C. & Emery, W. (2011) Distribution and trends in Arctic sea ice age through spring 2011.*Geophysical Research Letters*, **38**, L13502.

Maykut, G.A. (1985) *An Introduction to Ice in Polar Oceans. Reports of the Applied Physics Laboratory*. University of Washington, Seattle, WA.

Maykut, G.A., & Untersteiner, N. (1971) Some results from a time-dependent thermodynamic model of sea ice. *Journal of Geophysical Research*, **76**, 1550–1575.

McPhee, M.G. (1981) An analytic similarity theory for the planetary boundary layer stabilized by surface buoyancy. *Boundary-Layer Meteorology*, **21**, 325–339.

McPhee, M.G. (1988) Analysis and Prediction of Short-Term Ice Drift. *Journal of Offshore Mechanics and Arctic Engineering*, **110**, 7.

McPhee, M.G. (1990) Small Scale Processes. In: *Polar Oceanography, Part A Physical Science* (Ed. W.O. Smith), pp. 287–334. Academic Press, San Diego, CA.

McPhee, M.G. (1992) Turbulent heat flux in the upper ocean under sea ice. *Journal of Geophysical Research: Oceans*, **97**, 5365–5379.

McPhee, M.G. (1994) On the turbulent mixing length in the oceanic boundary layer. *Journal of Physical Oceanography*, **24**, 2014–2031.

McPhee, M.G. (2002) Turbulent stress at the ice/ocean interface and bottom surface hydraulic roughness during the SHEBA drift. *Journal of Geophysical Research: Oceans*, **107**(C10), 8037.

McPhee, M.G. (2004) A spectral technique for estimating turbulent stress, scalar flux magnitude, and eddy viscosity in the ocean boundary layer under pack ice. *Journal of Physical Oceanography*, **34**, 2180–2188.

McPhee, M.G. (2008a) Physics of early summer ice/ocean exchanges in the western Weddell Sea during ISPOL. *Deep Sea Research Part II*, **55**, 1075–1097.

McPhee, M.G. (2008b) *Air-Ice-Ocean Interaction Turbulent Ocean Boundary Layer Exchange Processes*, IX.Springer, New York.

McPhee, M.G. (2012) Advances in understanding ice–ocean stress during and since AIDJEX. *Cold Regions Science and Technology*, **76–77**, 24–36.

McPhee, M.G. (2013) Intensification of geostrophic currents in the Canada Basin, Arctic Ocean. *Journal of Climate*, **26**, 3130–3138.

McPhee, M.G. & Smith, J.D. (1976) Measurements of the turbulent boundary layer under pack ice. *Journal of Physical Oceanography*, **6**, 696–711.

McPhee, M.G. & Martinson, D.G. (1994) Turbulent mixing under drifting pack ice in the Weddell Sea. *Science*, **263**, 218–221.

McPhee, M.G. & Stanton, T.P. (1996) Turbulence in the statically unstable oceanic boundary layer under Arctic leads. *Journal of Geophysical Research: Oceans*, **101**, 6409–6428.

McPhee, M.G., Maykut, G.A. & Morison, J.H. (1987) Dynamics and thermodynamics of the ice/upper ocean system in the marginal ice zone of the Greenland Sea. *Journal of Geophysical Research: Oceans*, **92**, 7017–7031.

McPhee, M.G., Kottmeier, C. & Morison, J.H. (1999) Ocean heat flux in the central Weddell Sea during Winter. *Journal of Physical Oceanography*, **29**, 1166–1179.

McPhee, M.G., Morison, J.H. & Nilsen, F. (2008) Revisiting heat and salt exchange at the ice-ocean interface: Ocean flux and modeling considerations. *Journal of Geophysical Research: Oceans*, **113**, C06014.

Mellor, G.L. & Yamada, T. (1982) Development of a turbulence closure model for geophysical fluid problems. *Reviews of Geophysics*, **20**, 851–875.

Mellor, G.L., McPhee, M.G. & Steele, M. (1986) Ice-Seawater Turbulent Boundary Layer Interaction with Melting or Freezing. *Journal of Physical Oceanography*, **16**, 1829–1846.

Nghiem, S.V., Rigor, I.G., Perovich, D.K., Clemente-Colón, P., Weatherly, J.W.& Neumann, G. (2007) Rapid reduction of Arctic perennial sea ice. *Geophysical Research Letters*, **34**, L19504.

Niiler, P.P. & Kraus, E.B. (1977) One-dimensional models of the Upper Ocean. In: *Modelling and Prediction of the Upper Layers of the Ocean* (Ed. E.B. Kraus). Pergamon Press, Oxford.

Notz, D. & Worster, M.G. (2009) Desalination processes of sea ice revisited. *Journal of Geophysical Research: Oceans*, **114**, C05006.

Notz, D., McPhee, M.G., Worster, M.G. et al. (2003) Impact of underwater-ice evolution on Arctic summer sea ice, *Journal of Geophysical Research: Oceans*, **108**, 3223.

Obukhov, A.M. (1971) Turbulence in an atmosphere with a non-uniform temperature, *Boundary-Layer Meteorology*, **2**, 7–29.

Parkinson, C.L. & Washington, W.M. (1979) A large-scale numerical model of sea ice. *Journal of Geophysical Research: Oceans*, **84**, 311–337.

Pease, C.H., Salo, S.A. & Overland, J.E. (1983) Drag measurements for first-year sea ice over a shallow sea. *Journal of Geophysical Research: Oceans*, **88**, 2853–2862.

Pedlosky, J. (1987) *Geophysical fluid dynamics*, 2nd edn., **xiv**, Springer-Verlag, New York.

Perovich, D.K., Grenfell, T.C., Richter-Menge, J.A., Light, B., Tucker, W.B. & Eicken, H. (2003) Thin and thinner: Sea ice mass balance measurements during SHEBA. *Journal of Geophysical Research: Oceans*, **108**, 8050.

Pollard, R.T., Rhines, P.B. & Thompson, R.O. R.Y. (1973) The deepening of the wind mixed layer, *Geophysical Fluid Dynamics*, **3**, 381–404.

Price, J.F., Weller, R.A. & Pinkel, R. (1986) Diurnal cycling: Observations and models of the upper ocean response to diurnal heating, cooling, and wind mixing, *Journal of Geophysical Research: Oceans*, **91**, 8411–8427.

Robinson, N.J., Williams, M.J. M., Barrett, P.J. & Pyne, A.R. (2010) Observations of flow and ice-ocean interaction beneath the McMurdo Ice Shelf, Antarctica. *Journal of Geophysical Research: Oceans*, **115**, C03025.

Rossby, C.-G. & Montgomery, R.B. (1935) The layer of frictional influence in wind and water current. *Papers in Physical Oceanography and Meteorology, Massachusetts Institute of Technology and Woods Hole Oceanographic Institute*, **3**, 1–100.

Shaw, W.J., Stanton, T.P., McPhee, M.G. & Kikuchi, T. (2008), Estimates of surface roughness length in heterogeneous under-ice boundary layers, *Journal of Geophysical Research: Oceans*, **113**, C08030.

Shaw, W.J., Stanton, T.P., McPhee, M.G., Morison, J.H. & Martinson, D.G. (2009) Role of the upper ocean in the energy budget of Arctic sea ice during SHEBA. *Journal of Geophysical Research: Oceans*, **114**, C06012.

Shirasawa, K. (1986) Water stress and ocean current measurements under first-year sea ice in the Canadian Arctic. *Journal of Geophysical Research: Oceans*, **91**, 14305–14316.

Sirevaag, A. (2009) Turbulent exchange coefficients for the ice/ocean interface in case of rapid melting.*Geophysical Research Letters*, **36**, L04606.

Skyllingstad, E.D., Paulson, C.A., Pegau, W.S., McPhee, M.G. & Stanton, T. (2003) Effects of keels on ice bottom turbulence exchange, *Journal of Geophysical Research: Oceans*, **108**, 3372.

Steele, M., Mellor, G.L. & McPhee, M.G. (1989) Role of the molecular sublayer in the melting or freezing of sea ice. *Journal of Physical Oceanography*, **19**, 139–147.

Toole, J.M., Timmermans, M.L., Perovich, D.K., Krishfield, R.A., Proshutinsky, A. & Richter-Menge, J.A. (2010), Influences of the ocean surface mixed layer and thermohaline stratification on Arctic Sea ice in the central Canada Basin. *Journal of Geophysical Research: Oceans*, **115**, C10018.

Turner, J.S. (1973) *Buoyancy Effects in Fluids*, Cambridge University Press, Cambridge.

Untersteiner, N. (1961) On the mass and heat budget of Arctic sea ice. *Archives for Meteorology, Geophysics and Bioclimatology Series A*, **12**, 151–182.

Weeks, W.F & Ackley, S.F. (1986) The growth, structure, and properties of sea ice, in *The Geophysics of Sea Ice* (Ed. by N. Untersteiner), pp. 9–164, Plenum Press, New York.

Wettlaufer, J.S., Worster, M.G. &Huppert, H.E. (1997) The phase evolution of young sea ice. *Geophysical Research Letters*, **24**, 1251–1254.